

Evidence of a Type Ia Progenitor for Supernova Remnant 3C 397

Héctor Martínez-Rodríguez^{1*}, Laura A. Lopez^{2,3,4}, Katie Auchettl^{5,6,4,7}, Carles Badenes¹, Tyler Holland-Ashford², Daniel J. Patnaude⁸, Shiu-Hang Lee^{9,10}, Adam R. Foster⁸, Patrick O. Slane⁸

¹Department of Physics and Astronomy and Pittsburgh Particle Physics, Astrophysics and Cosmology Center (PITT PACC), University of Pittsburgh, 3941 O’Hara Street, Pittsburgh, PA 15260, USA

²Department of Astronomy, The Ohio State University, 140 W. 18th Ave., Columbus, Ohio 43210, USA

³Center for Cosmology and Astro-Particle Physics, The Ohio State University, 191 West Woodruff Avenue, Columbus, OH 43210, USA

⁴DARK, Niels Bohr Institute, University of Copenhagen, Lyngbyvej 2, 2100 Copenhagen, Denmark

⁵School of Physics, The University of Melbourne, Parkville, VIC 3010, Australia

⁶ARC Centre of Excellence for All Sky Astrophysics in 3 Dimensions (ASTRO 3D)

⁷Department of Astronomy and Astrophysics, University of California, Santa Cruz, CA 95064, USA

⁸Smithsonian Astrophysical Observatory, 60 Garden St, Cambridge, MA 02138

⁹Department of Astronomy, Kyoto University, Kyoto 606-8502, Japan

¹⁰RIKEN, Astrophysical Big Bang Laboratory, 2-1 Hirosawa, Wako, Saitama 351-0198, Japan

17 June 2020

ABSTRACT

The explosive origin of the young supernova remnant (SNR) 3C 397 (G41.1–0.3) is debated. Its elongated morphology and proximity to a molecular cloud are suggestive of a core-collapse (CC) SN origin, yet recent X-ray studies of heavy metals show chemical yields and line centroid energies consistent with a Type Ia SN. In this paper, we analyze the full X-ray spectrum from 0.7–10 keV of 3C 397 observed with *Suzaku* and compare the line centroid energies, fluxes, and elemental abundances of intermediate-mass and heavy metals (Mg to Ni) to Type Ia and CC hydrodynamical model predictions. Based on the results, we conclude that 3C 397 likely arises from an energetic Type Ia explosion in a high-density ambient medium, and we show that the progenitor was a near Chandrasekhar mass white dwarf.

Key words: atomic data, hydrodynamics, ISM: individual objects (3C 397, G41.1–0.3), ISM: supernova remnants, X-rays: ISM

1 INTRODUCTION

Supernovae (SNe) are stellar explosions divided into two main categories: core-collapse (CC) and Type Ia SNe. CC SNe arise from massive stars $\gtrsim 8 M_{\odot}$ that undergo CC when the iron core cannot be supported by nuclear fusion (e.g., Iben 1974; Eldridge & Tout 2004; Smartt 2009). SNe Ia are the thermonuclear explosions of a carbon-oxygen white dwarf (WD) triggered by mass transfer from a companion, which could be a non-degenerate hydrogen- or helium-burning star or another WD (see Maoz et al. 2014 for a review).

SNe are usually typed using their optical spectra around maximum light, days after explosion (see reviews by e.g.,

Filippenko 1997; Gal-Yam 2017), and hundreds of SNe are discovered per year through dedicated surveys (e.g. ASASSN: Shappee et al. 2014; Holien et al. 2017a,b,c, 2018; ATLAS: Tonry et al. 2018; Pan-STARRS: Flewelling et al. 2016; Chambers et al. 2016; Jones et al. 2018, ZTF: Smith et al. 2014; Dugas et al. 2018; Kulkarni 2018 and YSE: Jones et al. 2019). However, these objects are often too distant (~ 1 –100 Mpc) to resolve the SN ejecta and the environment of the progenitor star. In this context, supernova remnants (SNRs), which are the leftover structures of SNe that happened hundreds or thousands of years ago, provide a complementary close view of the explosive endpoint of stellar evolution.

In particular, SNRs give valuable information about SN progenitors. At X-ray wavelengths, strong emission lines from shocked SN ejecta can be used to probe the nucleosyn-

*Email:hector.mr@pitt.edu

thetic products (e.g. Badenes et al. 2008a; Park et al. 2013; Yamaguchi et al. 2015; Martínez-Rodríguez et al. 2017). Additionally, their X-ray spectra and morphologies depend on the ejecta, explosion energetics, and the surrounding circumstellar material left by the progenitor (e.g. Badenes et al. 2003, 2007; Lopez et al. 2009b, 2011; Patnaude et al. 2012, 2017; Woods et al. 2017, 2018). The most reliable ways to connect SNRs to their progenitors are via detection of an associated pulsar (Hewish et al. 1968; Tananbaum 1999) or through light echoes (e.g., Rest et al. 2005, 2008a,b). Another approach is to examine the stellar populations surrounding these sources (e.g., Badenes et al. 2009; Auchettl et al. 2019).

SNRs can also be typed from their abundance ratios (e.g., Reynolds et al. 2007; Katsuda et al. 2018), morphologies (Lopez et al. 2009b, 2011; Peters et al. 2013; Lopez & Fesen 2018), Fe-K centroids (Yamaguchi et al. 2014b), and absorption line studies (e.g., Hamilton & Fesen 2000; Fesen et al. 2017). However, even with these varied techniques, the explosive origin of some SNRs remain uncertain, such as the Milky Way SNR 3C 397 (G41.1–0.3). Safi-Harb et al. (2000) suggested that 3C 397 arose from a CC SN based on its proximity to molecular clouds and on enhanced abundances of intermediate-mass elements from *ASCA* observations. By contrast, Yamaguchi et al. (2014b) and Yamaguchi et al. (2015) found that a Type Ia origin was more likely, given 3C 397's Fe K-shell centroid and its exceptionally high abundances of neutron-rich, stable iron-group elements (Cr, Mn, Ni, Fe; though these elements have been detected in CC SNRs, e.g. Sato et al. 2020). Recent efforts to determine its progenitor metallicity (Dave et al. 2017; Martínez-Rodríguez et al. 2017) have assumed a Type Ia nature.

Although its exact age is uncertain, 3C 397 is likely $\sim 1350 - 5000$ years old (Safi-Harb et al. 2005; Leahy & Ranasinghe 2016), implying it is dynamically more evolved than other well-known Type Ia SNRs (e.g. G1.9+0.3, 0509–67.5, Tycho, Kepler, SN 1006). The X-ray emission from 3C 397 is thermal in nature without a non-thermal component (Yamaguchi et al. 2015), unlike some other Type Ia SNRs (e.g., G1.9+0.3: Zoglauer et al. 2015; Tycho: Lopez et al. 2015). Its X-ray morphology is quite irregular (Safi-Harb et al. 2005), and Lee et al. (2019) suggested that it likely results from interaction with a dense surrounding medium rather than an asymmetric explosion.

3C 397 is among the class of mixed-morphology SNRs (Rho & Petre 1998), which are center-filled in X-rays and have a shell-like morphology in the radio. 3C 397 is expanding into a high-density ambient medium (with $n_{\text{amb}} \sim 2 - 5 \text{ cm}^{-3}$; Leahy & Ranasinghe 2016), with a strong westward gradient. Although this environment is more consistent with a CC SNR, other Type Ia SNRs have signs of interaction: e.g., Tycho may be interacting with a nearby molecular cloud (Lee et al. 2004; Zhou et al. 2016), N103B has CO clouds along its southeastern edge (Sano et al. 2018).

In this paper, we aim to better constrain the explosive origin of 3C 397 using the observed emission in the full X-ray band (0.7–10 keV) and comparing it to synthetic SNR spectra generated from both Type Ia and CC explosion models. The paper is organized as follows. In Section 2, we present the X-ray observations of 3C 397 and the spectral-fitting process. In Section 3, we compare the observational

and synthetic results. Finally, in Section 4, we summarize the conclusions.

2 OBSERVATIONS AND DATA ANALYSIS

Following the previous studies by Yamaguchi et al. (2014b) and Yamaguchi et al. (2015), we take advantage of the high spectral resolution of the X-ray Imaging Spectrometer (XIS) on board *Suzaku* to measure the centroids and fluxes of all Ly α and K α emission lines. We analyze *Suzaku* observations 505008010 and 508001010, which were taken on 2010 October 24 and 2013 October 30, with total exposure times of 69 and 103 ks, respectively. We use HEASOFT version 2.12 and reprocess the unfiltered public data using the *aepipeline*, the most up-to-date calibration files, and the standard reduction procedures¹.

We extracted spectra from both the front- (XIS0, XIS3) and back-illuminated (XIS1) CCDs of the entire SNR using an elliptical region and XSELECT version 2.4d. For the background spectrum, we extracted spectra from the full field-of-view of the XIS observations, excluding the calibration regions and the SNR. To generate the redistribution matrix files (RMF) and ancillary response files (ARF), we use the standard *Suzaku* analysis tools *xisrmfgen* and *xisarfgen*, respectively. Due to an error with the ARF analysis pipeline, we are unable to extract a XIS1 spectrum from ObsID 508001010 and thus do not use this spectrum for our analysis. We also remove (from both the source and background spectra) the contribution of the non-X-ray (i.e., instrumental) background (NXB) that arises from charged particles and hard X-ray (Tawa et al. 2008) interacting with the detectors. To simulate the instrumental background, we use *xisnxbgen* (Tawa et al. 2008) to generate a NXB model and then subtract it from our source and background spectra, similar to what was done in, e.g., Auchettl et al. (2015).

Rather than merging the spectra together, we fit our background-subtracted spectra simultaneously using XSPEC² (Arnaud 1996, version 12.10.1) using the standard atomic database. We analyze a broad energy range (0.7 – 10.0 keV) to measure the centroids of all prominent Ly α and K α lines in the 3C 397 data. We model the X-ray continuum using two absorbed bremsstrahlung components (XSPEC model: TBABS*(BREMSS+BREMSS)), one soft (with temperature kT_s) and one hard (with temperature kT_h). For the emission lines, we include phenomenological Gaussian components with centroid energies, widths, and normalizations tied among the five source spectra. We freeze the column density to $N_{\text{H}} = 3.5 \times 10^{22} \text{ cm}^{-2}$ (as derived from our physical model listed in Table 3), similar to Yamaguchi et al. 2014b who used $N_{\text{H}} = 3 \times 10^{22} \text{ cm}^{-2}$ based on the results of Safi-Harb et al. 2005. We adopt solar abundance values from Wilms et al. (2000).

Tables 1 and 2 show the best-fit results, including the centroid energies, line fluxes, and the thermal plasma properties. The spectra and the mean best-fit model for 3C 397 are shown in Figure 1. Yamaguchi et al. (2015), who modeled the 5–9 keV spectrum from *Suzaku* to focus on the Fe-peak

¹ <http://heasarc.nasa.gov/docs/suzaku/processing/criteriaxis.html>

² <https://heasarc.gsfc.nasa.gov/xanadu/xspec/manual/>

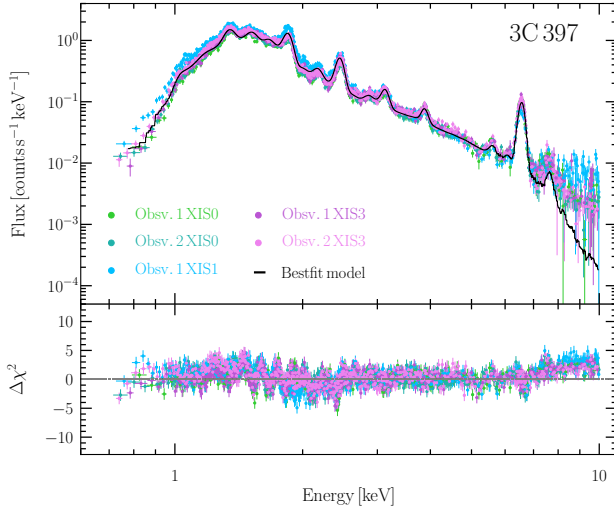


Figure 1. The five background-subtracted *Suzaku* X-ray spectra of 3C 397, the best-fit model (as listed in Tables 1 and 2), and the associated residuals.

elements, derived fluxes for several emission lines common to our analysis: Cr K α , Mn K α , Fe K α , and Ni K α + Fe K β . Our centroid energies and fluxes are comparable to those measured by Yamaguchi et al. (2015), except our Ni K α + Fe K β centroid energy is 31 eV lower ($\sim 1.2 \sigma$) and flux is $\approx 60\%$ greater than that previous work. This is likely a result of the different continuum temperatures used by Yamaguchi et al. (2015) and in this analysis (~ 2.1 keV versus ~ 1.6 keV, respectively), and the fact that we used two components rather than one to model the X-ray emission of the SNR. However, these differences between Yamaguchi et al. (2015) and our work do not affect our conclusions.

3 RESULTS AND DISCUSSION

3.1 Explosive Origin Constraints from Line Ratios and Centroid Energies

We compare the observational fluxes reported in Table 1 with theoretical models for the X-ray spectra of both Type Ia and CC SNRs. In contrast to Yamaguchi et al. (2015), who focused on the $M_{\text{Mn}}/M_{\text{Fe}}$ and $M_{\text{Ni}}/M_{\text{Fe}}$ mass ratios, we examine a broader range of metals that includes both intermediate-mass and Fe-peak elements.

We use a grid of synthetic X-ray spectra (see Martínez-Rodríguez et al. 2018, for a detailed explanation) for Type Ia SN models that assume a progenitor with a metallicity of $Z = 0.009$ ($\approx 0.64 Z_{\odot}$) which is expanding into the SNR phase, similar to that used in previous studies of Type Ia SNRs (e.g., Badenes et al. 2003, 2005, 2008b; Martínez-Rodríguez et al. 2018). We analyze the synthetic spectra from the X-ray emitting ejecta in M_{Ch} and sub- M_{Ch} models (Bravo et al. 2019), adopting three uniform ambient medium densities: $\rho_{\text{amb}} = 10^{-24}$, 2×10^{-24} , and $5 \times 10^{-24} \text{ g cm}^{-3}$ (corresponding to ambient number densities of $n_{\text{amb}} = 1$, 2, and 5.0 cm^{-3}). These values are consistent with the estimated densities around 3C 397 of $n_{\text{amb}} \sim 2-5 \text{ cm}^{-3}$ (Leahy & Ranasinghe 2016).

Table 1. Best-fit model line parameters for the combined *Suzaku* spectra of 3C 397. All uncertainties are 90% confidence intervals.

Transition	Centroid energy (eV)	$\langle \text{Flux} \rangle$ ($\text{ph cm}^{-2} \text{s}^{-1}$)
Ne Ly α	1027^{+5}_{-4}	$(1.22^{+01.3}_{-1.2}) \times 10^{-2}$
Mg K α	1345^{+1}_{-1}	$(4.03^{+0.12}_{-0.12}) \times 10^{-3}$
Si K α	1853^{+1}_{-1}	$(1.78^{+0.03}_{-0.03}) \times 10^{-3}$
Si K β	2218^{+4}_{-6}	$(9.13^{+0.70}_{-0.70}) \times 10^{-5}$
S K α	2454^{+1}_{-1}	$(5.15^{+0.10}_{-0.10}) \times 10^{-4}$
Ar K α	3124^{+4}_{-4}	$(7.11^{+0.40}_{-0.40}) \times 10^{-5}$
Ca K α	3878^{+9}_{-6}	$(2.01^{+0.20}_{-0.20}) \times 10^{-5}$
Cr K α	5601^{+12}_{-11}	$(1.00^{+0.10}_{-0.10}) \times 10^{-5}$
Mn K α	6061^{+21}_{-13}	$(7.3^{+0.96}_{-0.84}) \times 10^{-6}$
Fe K α	6552^{+3}_{-2}	$(1.39^{+0.03}_{-0.03}) \times 10^{-4}$
Ni K α + Fe K β	7585^{+13}_{-12}	$(2.61^{+0.14}_{-0.14}) \times 10^{-5}$

Table 2. Best-fit N_{H} and bremsstrahlung components in phenomenological spectral fit. All uncertainties are 90% confidence intervals.

N_{H} (10^{22} cm^{-2})	kT_s (keV)	Norm $_{\text{s}}^{\text{a}}$	kT_h (keV)	Norm $_{\text{h}}^{\text{a}}$
3.49 [frozen]	0.24 ± 0.01	$14.0^{+0.7}_{-0.6}$	1.60 ± 0.03	0.02 ± 0.001

^a The normalizations Norm $_{\text{s}}$ and Norm $_{\text{h}}$ are given in units of $(10^{-14}/4\pi D^2) \int n_{\text{e}} n_{\text{H}} dV$ (cm^{-5}), where D is the distance to the source (cm), n_{e} and n_{H} are the electron and hydrogen densities (cm^{-3}), respectively.

In addition, we consider synthetic X-ray spectra from single-star CC explosion models (specifically, models s25D and s12D from Heger & Woosley 2010) and adopted in previous SNR studies (Lee et al. 2014; Patnaude et al. 2015). In total, we produce eight SNR models using two sets of mass-loss rates and wind velocities ($10^{-5} M_{\odot} \text{ yr}^{-1}$, 10 km s^{-1} and $2 \times 10^{-5} M_{\odot} \text{ yr}^{-1}$, 20 km s^{-1}) and four CC SN ejecta profiles. The four ejecta profiles are from two stars with initial masses of 12 and 25 M_{\odot} (that lose ~ 3 and $13 M_{\odot}$, respectively, by the onset of CC), a 6 M_{\odot} He star enclosed in a $10 M_{\odot}$ H envelope (tailored to mimic SN 1987A), and a 18 M_{\odot} main-sequence star with a mass-loss of $15 M_{\odot}$ by CC (matched to Type IIb SN 1993J). We note that while this set

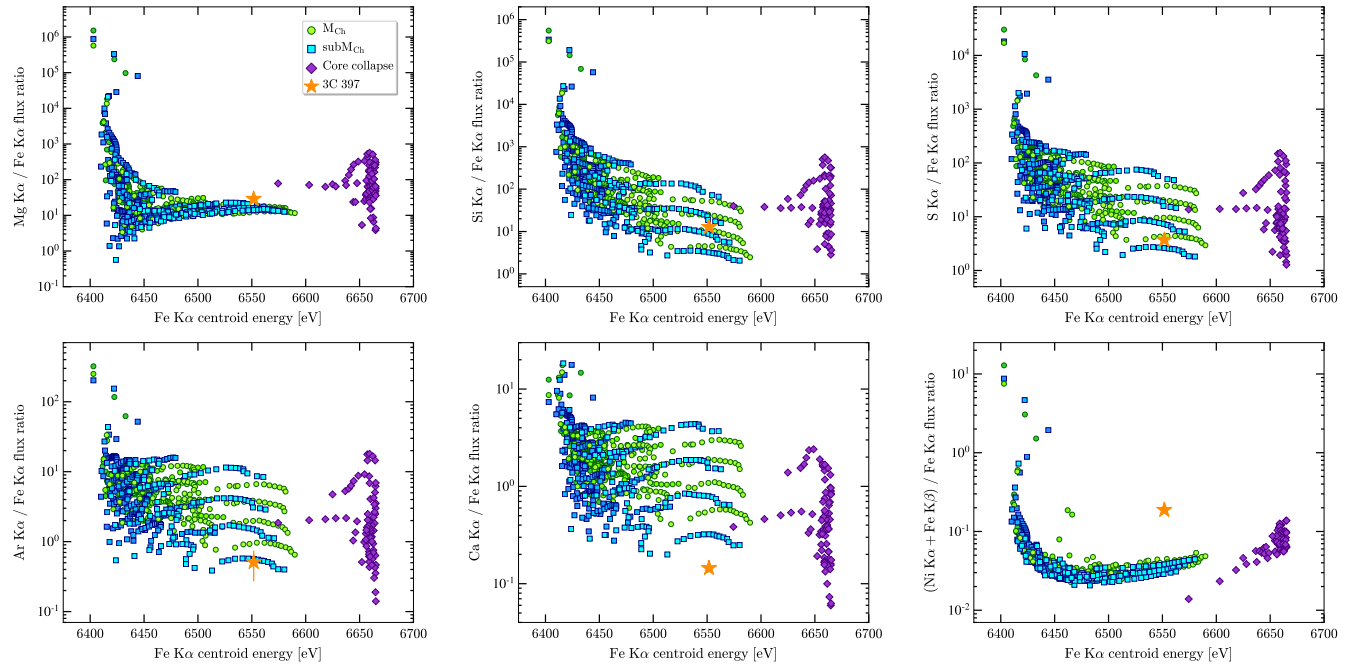


Figure 2. Emission line fluxes normalized to the Fe $K\alpha$ flux versus Fe $K\alpha$ centroid energy for the M_{Ch} models (green circles), sub- M_{Ch} models (blue squares), CC models (purple diamonds; from Patnaude et al. 2015), and observed from 3C 397 (orange star). Lighter shades of blue and green correspond to greater ambient densities.

of CC SNR models is not comprehensive, it is diverse enough to be representative and has been shown to provide a good match to the bulk dynamics of most CC SNRs (Patnaude et al. 2015, 2017).

We calculate centroid energies and line fluxes from the unconvolved, differential photon fluxes of these SNR model spectra using Equations 2 and 3 of Martínez-Rodríguez et al. (2018). For each transition, we select the energy integration range from the 3σ limit of the corresponding Gaussian profile in the convolved *Suzaku* spectra.

Figure 2 shows the emission line ratios (relative to Fe $K\alpha$) versus the Fe $K\alpha$ centroid energy derived from the synthetic spectra. We normalize the ratios relative to Fe $K\alpha$ because that line is detected in many SNRs and is useful to characterize SN progenitors (Yamaguchi et al. 2014b; Patnaude et al. 2015; Patnaude & Badenes 2017; Martínez-Rodríguez et al. 2018). In SNRs, the Fe $K\alpha$ flux is sensitive to the electron temperature and ionization timescale, and the Fe $K\alpha$ centroid energy is an excellent tracer of the mean charge state of Fe (Vink 2012; Yamaguchi et al. 2014a,b). As a consequence, the latter can be used to distinguish whether SNRs arise from Type Ia and CC SNe (Yamaguchi et al. 2014b), with the former having centroids <6550 eV and the latter having centroids >6550 eV. We find that 3C 397 has a Fe $K\alpha$ centroid of 6552^{+3}_{-2} eV, consistent with the value derived by Yamaguchi et al. (2014b) of 6556^{+4}_{-3} eV and at the boundary that distinguishes Type Ia from CC progenitors.

² We note that one possible exception is the SNR W49B, which has a Fe $K\alpha$ centroid of 6663 ± 1 eV reported by Yamaguchi et al. (2014b), and it is debated whether the originating explosion was a Type Ia (Zhou & Vink 2018) or CC SN (Lopez et al. 2009a, 2013a).

We find that at the measured value of the Fe $K\alpha$ centroid, the observed line flux ratios derived for 3C 397 are broadly consistent with the Type Ia M_{Ch} and sub- M_{Ch} models and are incompatible with the CC models. The Mg/Fe flux ratio of 3C 397 is $\sim 50\%$ greater than our Type Ia model predictions, but the Si/Fe, S/Fe, and Ar/Fe flux ratios are consistent with both Type Ia scenarios as long as $\rho_{amb} \gtrsim (2.0 - 5.0) \times 10^{-24} \text{ g cm}^{-3}$.

The Ca/Fe flux ratio in 3C 397 is $\sim 2.5 \times$ below our model predictions. Previous studies comparing the derived emission properties of Ca $K\alpha$ to hydrodynamical models have found similar inconsistencies. For example, Martínez-Rodríguez et al. (2017) showed that the Ca/S mass ratio measured from X-ray spectra of Type Ia SNRs cannot be reproduced with the standard reaction rates used in most SN Ia explosion models. Both Yamaguchi et al. (2015) and Martínez-Rodríguez et al. (2017) pointed out that the $(\text{Ni } K\alpha + \text{Fe } K\beta)/\text{Fe } K\alpha$ flux ratio is exceptionally large for a Type Ia SNR. Martínez-Rodríguez et al. (2017) showed that this large ratio is suggestive of a high-metallicity progenitor, which may also explain the anomalous Ca/Fe ratios seen for 3C 397.

We note that discrepancies between the observed values and the models may be due to well-documented challenges in comparing simple explosion models to an entire X-ray spectrum. For example, one-dimensional hydrodynamic models cannot account for variations in interstellar absorption, non-thermal contribution, and background across the SNR (see Badenes et al. 2003 and Badenes et al. 2006).

Figure 3 shows the theoretical and observational centroid energies for the transitions depicted in Figure 2. These centroids tend to have higher energies for greater expansion ages and ambient densities. For Mg and Si, the observed values in 3C 397 are consistent with both M_{Ch} and sub- M_{Ch}

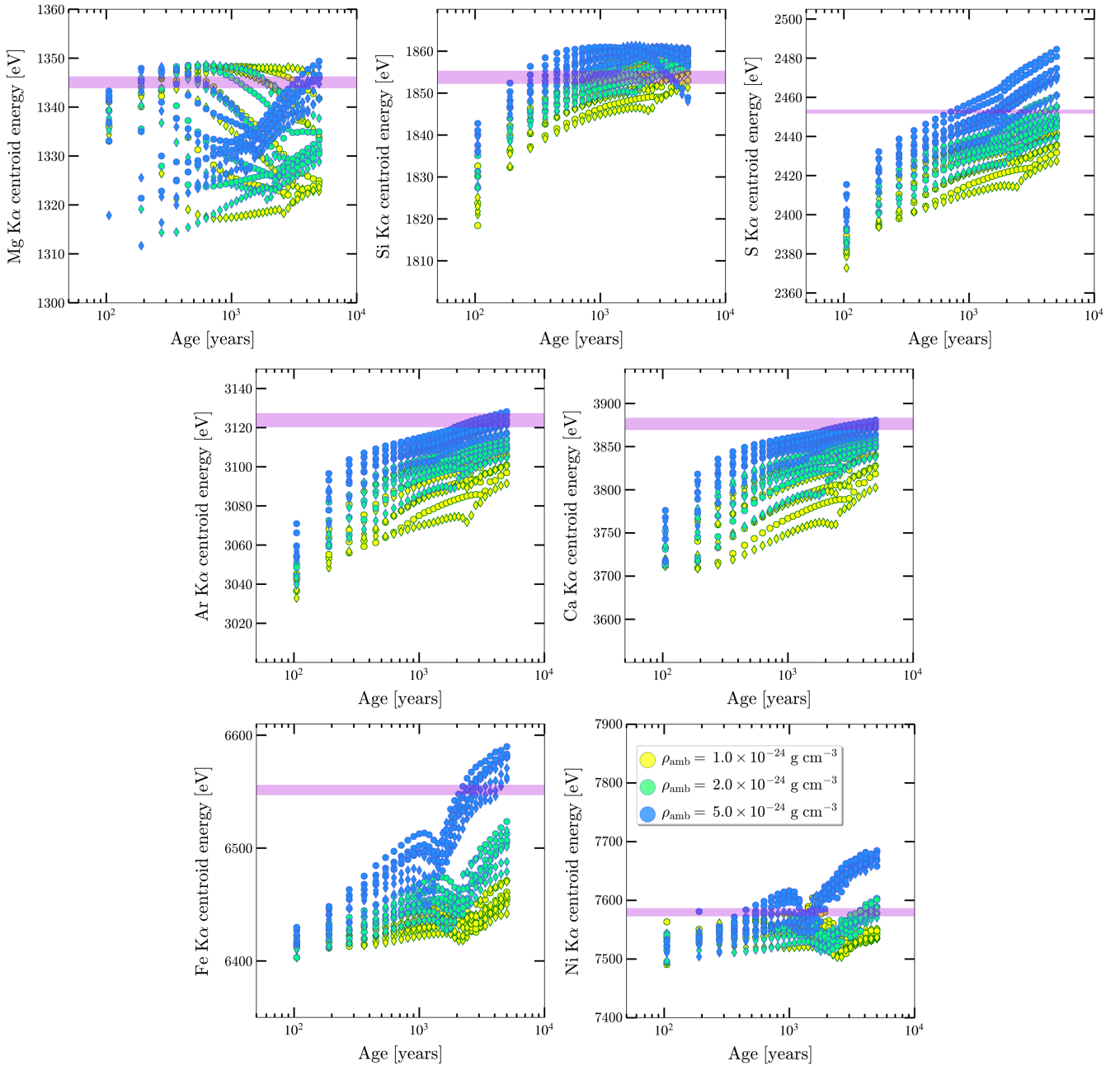


Figure 3. Emission-line centroid energies versus expansion age for the M_{Ch} models (circles), sub- M_{Ch} models (diamonds) of different ambient densities: $\rho_{\text{amb}} = [1.0, 2.0, 5.0] \times 10^{-24} \text{ g cm}^{-3}$. The shaded purple region corresponds to the best-fit emission-line centroid of 3C397 as derived in Table 1.

Type Ia models of medium ambient densities and a wide range of ages ($\gtrsim 200 - 5000$ years). The centroid energies of S, Ar, Ca, Fe and Ni are more consistent with the highest ambient medium densities ($\rho_{\text{amb}} = 5.0 \times 10^{-24} \text{ g cm}^{-3}$), suggesting that 3C 397 is in a dense environment, consistent with that found by Leahy & Ranasinghe (2016) and its irregular morphology (Lee et al. 2019). While the centroid energies of S, Ar, and Ni can occur over a wide range of ages ($\gtrsim 700 - 5000$ years), the Ca and Fe centroids set the most stringent constraints. Our results suggest that 3C 397 has an age between 2000–4000 years, consistent with (but more constraining than) estimates reported in the litera-

ture (1350–5300 years: Safi-Harb et al. 2000, 2005; Leahy & Ranasinghe 2016, 2018).

To further explore the ionization state of the plasma, we extract the centroid energy as a function of the parent ion charge for all of the observed K α transitions listed in Table 1 (Mg, Si, S, Ar, Ca, Cr, Mn, Fe and Ni) using the *AtomDB* database (Foster et al. 2012, 2014). Figure 4 shows these centroid energies and the values measured for 3C 397, including the corresponding ionization state for each transition. The derived centroids suggest that the plasma of 3C 397 is highly (but not fully) ionized, and the charge number of the Fe-peak elements saturates at an ion charge of 20. These values are

at the extreme end of observations of other Type Ia SNRs, though they are still lower than those found for CC SNRs (c.f., Figure 1 of Yamaguchi et al. 2014a), supporting the Type Ia progenitor origin of 3C 397.

3.2 Explosive Origin Constraints from Plasma Ionization State and Metal Abundances

To further probe the explosive origin of 3C 397, we search for evidence of overionization (recombination) by fitting the 0.7 – 10 keV spectrum with multiple non-equilibrium ionization (NEI) model components (VVRNEI). Overionization is a signature of rapid cooling that causes the ions to be stripped of more electrons than expected for the observed electron temperature of the plasma. This rapid cooling could arise from thermal conduction (Kawasaki et al. 2002b), adiabatic expansion (Itoh & Masai 1989), or interaction with dense material (Dwarkadas 2005). To date, overionization has only been detected in mixed-morphology SNRs (e.g., W49B: Kawasaki et al. 2005; Ozawa et al. 2009; Miceli et al. 2010; Lopez et al. 2013b; IC443: Kawasaki et al. 2002a, 2005; Yamaguchi et al. 2009; Ohnishi et al. 2014; Matsumura et al. 2017), many of which have been classified as CC SNRs based on their elemental abundances, their morphologies, and the dense material in their environments.

We find that the ejecta emission of 3C 397 is best described by an underionized plasma, where the temperature of the electrons is greater than the ionization temperature, contrary to an overionized plasma. However, we note that the absence of overionization does not exclude a CC origin, since many CC SNRs (such as Cassiopeia A: Hughes et al. 2000) are also underionized.

Finally, we aim to constrain the explosive origin of 3C 397 based on the abundance ratios from the 0.7 – 10 keV *Suzaku* spectra. Safi-Harb et al. (2005) analyzed a 66 ks *Chandra* observation of 3C 397 and found that the emission was ejecta-dominated and best fit by two NEI plasma components. However, due to low signal-to-noise, the derived metal abundances (e.g., of Si and Fe) were not well constrained. Subsequent work using the *Suzaku* observations of 3C 397 analyzed specific energy bands (e.g., 2–5 keV: Martínez-Rodríguez et al. 2017; 5–9 keV: Yamaguchi et al. 2014b, 2015) rather than the full X-ray spectrum.

We find that three absorbed NEI plasma ($\text{TBABS}^*(\text{NEI}+\text{VNEI}+\text{VVNEI})$) components best describe the spectra of 3C 397 (see Table 3 for the best-fit parameters). Here, we let the column density N_{H} , ionisation timescale τ , normalisation, and temperatures of each NEI component be free parameters. Due to the strong emission lines from Si, S, Ar, Ca, Cr, Mn, Fe, and Ni, the abundances of these elements were also allowed to vary, while all other elements in each component were set to solar. We find that the two hottest components have super-solar abundances and are associated with ejecta, whereas the coolest component has ISM (solar) abundances. The ionisation timescale of the ISM component was frozen to $\tau = 5 \times 10^{13} \text{ s cm}^{-3}$ as this parameter was unconstrained. We also add three Gaussians, two with centroid energies of 1.01 ± 0.03 and 1.23 ± 0.02 keV to compensate for large residuals that correspond to Ne Ly α and Ne x (or Fe XXI), respectively (Foster et al. 2012, 2014). It is possible that the Ne could be at a different temperature or ionization to the rest of

Table 3. The best-fit parameters from physical model of spectra. All uncertainties are 90% confidence intervals.

Component	Parameter	Value
tbabs	$N_{\text{H}} (\times 10^{22} \text{ cm}^{-2})$	$3.49^{+0.02}_{-0.04}$
nei	kT_s (keV)	0.22 ± 0.02
	$\tau (\times 10^{13} \text{ s cm}^{-3})$	5.00 [frozen]
	normalization ^a ($\times 10^{-1}$)	7.65 ± 0.6
vnei	kT_s (keV)	0.58 ± 0.01
	Si	$3.37^{+0.11}_{-0.09}$
	S	$4.28^{+0.10}_{-0.14}$
	Ar	$6.56^{+0.60}_{-1.00}$
	Ca	$12.4^{+2.0}_{-3.0}$
	$\tau (\times 10^{11} \text{ s cm}^{-3})$	$4.07^{+0.59}_{-0.49}$
	normalization ^a ($\times 10^{-2}$)	5.8 ± 0.1
vvnei	kT_h (keV)	1.89 ± 0.03
	Cr	$25.3^{+4.1}_{-4.2}$
	Mn	$57.7^{+9.3}_{-12}$
	Fe	$13.2^{+0.4}_{-0.7}$
	Ni	$62.7^{+3.3}_{-6.2}$
	$\tau (\times 10^{11} \text{ s cm}^{-3})$	$1.05^{+0.4}_{-0.1}$
	normalization ^a ($\times 10^{-2}$)	1.7 ± 0.1
	χ^2_{reduced}	1.89

^a The normalizations are given in units of $(10^{-14}/4\pi D^2) \int n_e n_{\text{H}} dV$ (cm^{-5}), where D is the distance to the source (cm), n_e and n_{H} are the electron and hydrogen densities (cm^{-3}), respectively.

the plasma, causing it to not be fully captured by our NEI models. The third Gaussian, with a centroid energy of 6.43 ± 0.01 keV, accounts for the low centroid of the Fe K α emission line in 3C 397, which is less than the ~ 6.7 keV Fe peak energy assumed in the vnei/vvnei components. With the addition of the three Gaussians, our best fit yields $\chi^2_{\text{reduced}} = 1.89$.

We find super-solar abundances of metals in the two hottest components, with some elements (e.g., Cr, Mn, Ni) extremely enhanced relative to others (e.g., Fe). Super-solar abundances and ejecta-dominated emission is common among mixed-morphology SNRs (e.g., Lazendic & Slane 2006; Uchida et al. 2012; Auchettl et al. 2014, 2015). However, the extreme abundances of the Fe peak elements (Yamaguchi et al. 2015; Martínez-Rodríguez et al. 2017) suggested that 3C 397 arose from a Chandrasekhar mass progenitor that produced significant neutron-rich material during the explosion.

We calculate the X-ray emitting mass swept-up M_X by the forward shock of 3C 397 using $M_X = 1.4 m_{\text{H}} n_{\text{H}} f V$, where m_{H} and n_{H} is the mass and number density of hydrogen, V is the volume, and f is the filling factor. We adopt a distance to the SNR of $D = 8.5$ kpc (Ranasinghe & Leahy 2018) and a radius of $2.5' \approx 6.2$ pc. Based on the best-fit normalization of the ISM plasma and assuming $n_e = 1.2 n_{\text{H}}$, we find $n_{\text{H}} = 4.4 \text{ cm}^{-2}$, consistent with previous measurements in the literature (Leahy & Ranasinghe 2016) and the results from Section 3. The corresponding M_X is $148 d^{5/2} f^{1/2} M_{\odot}$ (where d is the distance scaled to 8.5 kpc), suggesting the SNR is in the Sedov-Taylor phase.

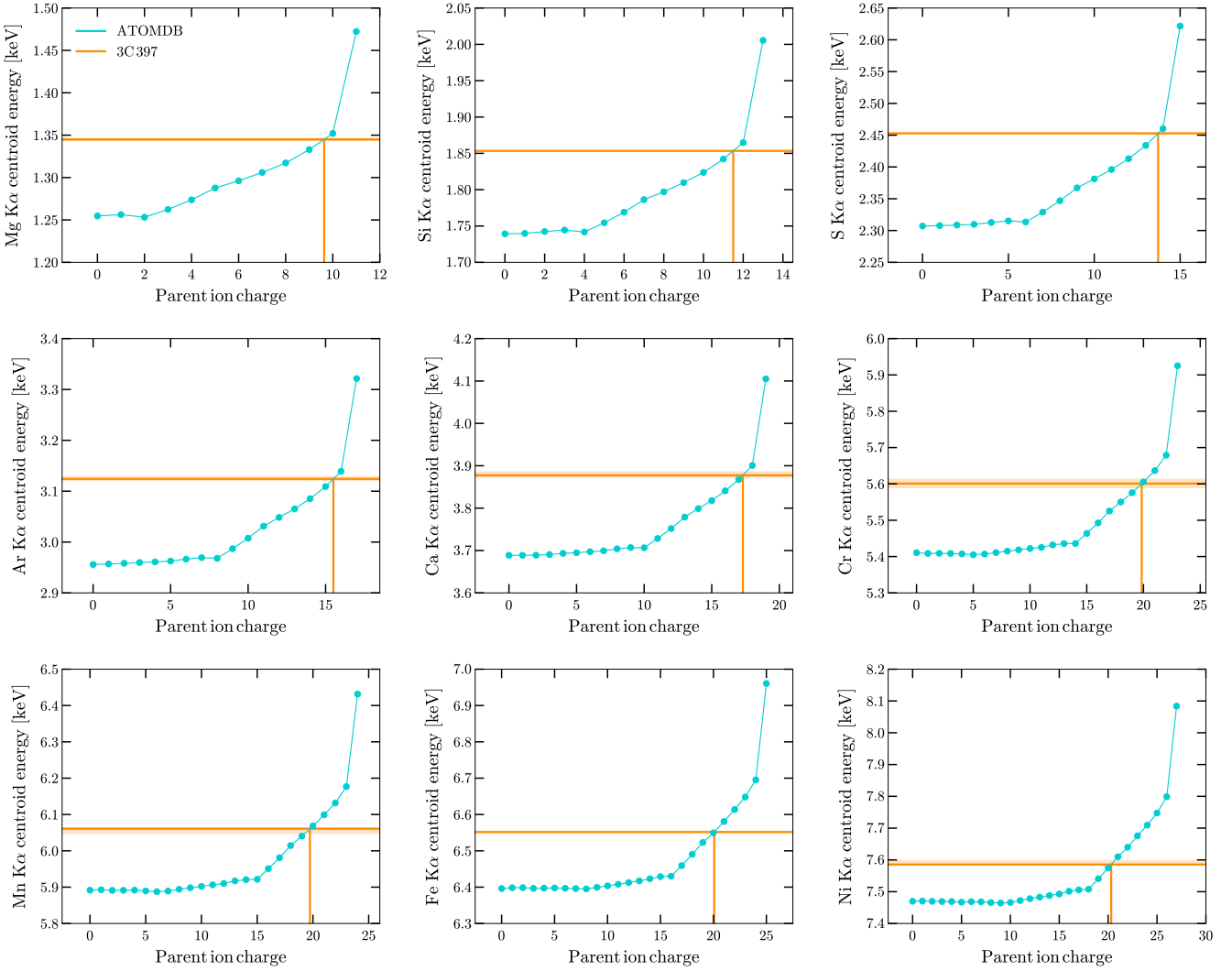


Figure 4. $K\alpha$ emission line centroid energies versus ion parent charge (charge number) from the *AtomDB* database. The best-fit values for 3C 397 (Table 1) are shown as orange shaded regions. The Fe-peak elements are more ionized than the intermediate-mass elements and are more consistent with Type Ia progenitor.

Assuming that the reverse shock has heated all of the ejecta, we estimate the mass of ejecta by summing the mass of each element M_i given the measured abundances: $M_i = [(a_i - 1)/1.4](n_i/n_H)(m_i/m_H)M_{\text{tot}}$. Here a_i is the abundance of element i listed in Table 3, m_i is the atomic mass of element i , n_i/n_H is its ISM abundance relative to hydrogen, and M_{tot} is the total mass of the ejecta thermal components. Based on the abundances in Table 3, we find that an ejecta mass of $\sim 1.22 d^{5/2} f^{1/2} M_{\odot}$, consistent with a Type Ia explosive origin.

From the abundances listed in Table 3, we calculate the mass ratios $M_{\text{Fe}}/M_{\text{S}} = 11.7^{+0.3}_{-0.2}$ and $M_{\text{Si}}/M_{\text{S}} = 1.05 \pm 0.01$. Here we have assumed that all ejecta have been shocked. These values are consistent with those of our most energetic sub- M_{Ch} Type Ia SN models, whereas the $M_{\text{Fe}}/M_{\text{S}}$ from our fits is $\gtrsim 5\times$ the predictions from CC models of Patnaude et al. (2015) and Sukhbold et al. (2016). The $M_{\text{Si}}/M_{\text{Fe}}$ ratio can be used to constrain the white dwarf progenitor mass (McWilliam et al. 2018). We find $M_{\text{Si}}/M_{\text{Fe}} = 0.09 \pm 0.002$ for 3C 397, which corresponds

to a $\sim 1.06\text{--}1.15 M_{\odot}$ white dwarf from the Bravo models presented in McWilliam et al. (2018). Yamaguchi et al. (2015) ruled out sub- M_{Ch} models for 3C 397 based on the Ni/Fe and Mn/Fe mass ratios, and our result is consistent with that conclusion.

4 CONCLUSIONS

We analyze the *Suzaku* X-ray observations of SNR 3C 397 to constrain its explosive origin. We measure the centroid energies and line fluxes using a phenomenological model, and we compare the values to those derived from synthetic spectra produced by Type Ia and CC explosion models. We find 3C 397 is most consistent with a Type Ia SN scenario that occurred in a high-density ambient medium ($\rho_{\text{amb}} \gtrsim 2\text{--}5 \times 10^{-24} \text{ g cm}^{-3}$) $\approx 2000\text{--}4000$ years ago. We model the 0.7 – 10 keV X-ray spectra using multiple NEI components, and we find that the ejecta are underionized and have super-solar abundances consistent with a Type

Ia origin. Finally, we calculate elemental mass ratios and compare to Type Ia and CC models. We show that these ratios are consistent with the former, and the $M_{\text{Si}}/M_{\text{Fe}}$ ratio suggests a white dwarf progenitor near M_{Ch} .

ACKNOWLEDGMENTS

Support for this work has been provided by the Chandra Theory award TM8-19004X. H.M.-R. acknowledges funding as a CCAPP Price Visiting Scholar, supported by the Dr. Pliny A. and Margaret H. Price Endowment Fund. H.M.-R. also acknowledges support from the NASA ADAP grant NNX15AM03G S01, a PITT PACC, a Zaccus Daniel and a Kenneth P. Dietrich School of Arts & Sciences Predoctoral Fellowship. KAA is supported by the Danish National Research Foundation (DNRF132). This research has made use of NASA's Astrophysics Data System (ADS, <http://adswww.harvard.edu/>). Parts of this research were supported by the Australian Research Council Centre of Excellence for All Sky Astrophysics in 3 Dimensions (ASTRO 3D), through project number CE170100013.

Software: FTOOLS (Blackburn 1995), XSPEC (Arnaud 1996), SAOIMAGE DS9 (Joye & Mandel 2003), ChN (Ellison et al. 2007; Patnaude et al. 2009; Ellison et al. 2010; Patnaude et al. 2010; Castro et al. 2012; Lee et al. 2014, 2015), Matplotlib (Hunter 2007), IPython (Pérez & Granger 2007), Numpy (Van Der Walt et al. 2011), PyAtomDB (<http://atomdb.readthedocs.io/en/master/>), Astropy (Astropy Collaboration et al. 2013; Price-Whelan et al. 2018), Python (<https://www.python.org/>), SciPy (<https://www.scipy.org/>).

REFERENCES

- Arnaud K. A., 1996, in Jacoby G. H., Barnes J., eds, Astronomical Society of the Pacific Conference Series Vol. 101, Astronomical Data Analysis Software and Systems V. p. 17
- Astropy Collaboration et al., 2013, *A&A*, **558**, A33
- Auchettl K., Slane P., Castro D., 2014, *ApJ*, **783**, 32
- Auchettl K., Slane P., Castro D., Foster A. R., Smith R. K., 2015, *ApJ*, **810**, 43
- Auchettl K., Lopez L. A., Badenes C., Ramirez-Ruiz E., Beacom J. F., Holland -Ashford T., 2019, *ApJ*, **871**, 64
- Badenes C., Bravo E., Borkowski K. J., Domínguez I., 2003, *ApJ*, **593**, 358
- Badenes C., Borkowski K. J., Bravo E., 2005, *ApJ*, **624**, 198
- Badenes C., Borkowski K. J., Hughes J. P., Hwang U., Bravo E., 2006, *ApJ*, **645**, 1373
- Badenes C., Hughes J. P., Bravo E., Langer N., 2007, *ApJ*, **662**, 472
- Badenes C., Bravo E., Hughes J. P., 2008a, *ApJ*, **680**, L33
- Badenes C., Hughes J. P., Cassam-Chenaï G., Bravo E., 2008b, *ApJ*, **680**, 1149
- Badenes C., Harris J., Zaritsky D., Prieto J. L., 2009, *ApJ*, **700**, 727
- Blackburn J. K., 1995, in Shaw R. A., Payne H. E., Hayes J. J. E., eds, Astronomical Society of the Pacific Conference Series Vol. 77, Astronomical Data Analysis Software and Systems IV. p. 367
- Bravo E., Badenes C., Martínez-Rodríguez H., 2019, *MNRAS*, **482**, 4346
- Castro D., Slane P., Ellison D. C., Patnaude D. J., 2012, *ApJ*, **756**, 88
- Chambers K. C., et al., 2016, arXiv e-prints, p. [arXiv:1612.05560](https://arxiv.org/abs/1612.05560)
- Dave P., Kashyap R., Fisher R., Timmes F., Townsley D., Byrohl C., 2017, *ApJ*, **841**, 58
- Dugas A., et al., 2018, The Astronomer's Telegram, **12065**
- Dwarkadas V. V., 2005, *ApJ*, **630**, 892
- Eldridge J. J., Tout C. A., 2004, *MNRAS*, **353**, 87
- Ellison D. C., Patnaude D. J., Slane P., Blasi P., Gabici S., 2007, *ApJ*, **661**, 879
- Ellison D. C., Patnaude D. J., Slane P., Raymond J., 2010, *ApJ*, **712**, 287
- Fesen R. A., Weil K. E., Hamilton A. J. S., Höflich P. A., 2017, *ApJ*, **848**, 130
- Filippenko A. V., 1997, *ARA&A*, **35**, 309
- Flewelling H. A., et al., 2016, arXiv e-prints, p. [arXiv:1612.05243](https://arxiv.org/abs/1612.05243)
- Foster A. R., Ji L., Smith R. K., Brickhouse N. S., 2012, *ApJ*, **756**, 128
- Foster A., Smith R. K., Yamaguchi H., Ji L., Wilms J., 2014, in American Astronomical Society Meeting Abstracts #223. p. 232.03
- Gal-Yam A., 2017, Observational and Physical Classification of Supernovae. p. 195, doi:10.1007/978-3-319-21846-5_35
- Hamilton A. J. S., Fesen R. A., 2000, *ApJ*, **542**, 779
- Heger A., Woosley S. E., 2010, *ApJ*, **724**, 341
- Hewish A., Bell S. J., Pilkington J. D. H., Scott P. F., Collins R. A., 1968, *Nature*, **217**, 709
- Holoien T. W.-S., et al., 2017a, *MNRAS*, **464**, 2672
- Holoien T. W.-S., et al., 2017b, *MNRAS*, **467**, 1098
- Holoien T. W.-S., et al., 2017c, *MNRAS*, **471**, 4966
- Holoien T. W. S., et al., 2018, arXiv e-prints, p. [arXiv:1811.08904](https://arxiv.org/abs/1811.08904)
- Hughes J. P., Rakowski C. E., Burrows D. N., Slane P. O., 2000, *ApJ*, **528**, L109
- Hunter J. D., 2007, Computing in Science and Engineering, **9**, 90
- Iben Jr. I., 1974, *ARA&A*, **12**, 215
- Itoh H., Masai K., 1989, *MNRAS*, **236**, 885
- Jones D. O., et al., 2018, *ApJ*, **857**, 51
- Jones D. O., et al., 2019, The Astronomer's Telegram, **13330**, 1
- Joye W. A., Mandel E., 2003, in Payne H. E., Jedrzejewski R. I., Hook R. N., eds, Astronomical Society of the Pacific Conference Series Vol. 295, Astronomical Data Analysis Software and Systems XII. p. 489
- Katsuda S., Takiwaki T., Tominaga N., Moriya T. J., Nakamura K., 2018, *ApJ*, **863**, 127
- Kawasaki M. T., Ozaki M., Nagase F., Masai K., Ishida M., Petre R., 2002a, *ApJ*, **572**, 897
- Kawasaki M. T., Ozaki M., Nagase F., Masai K., Ishida M., Petre R., 2002b, *ApJ*, **572**, 897
- Kawasaki M., Ozaki M., Nagase F., Inoue H., Petre R., 2005, *ApJ*, **631**, 935
- Kulkarni S. R., 2018, The Astronomer's Telegram, **11266**
- Lazendic J. S., Slane P. O., 2006, *ApJ*, **647**, 350
- Leahy D. A., Ranasinghe S., 2016, *ApJ*, **817**, 74
- Leahy D. A., Ranasinghe S., 2018, *ApJ*, **866**, 9
- Lee J.-J., Koo B.-C., Tatematsu K., 2004, *ApJ*, **605**, L113
- Lee S.-H., Patnaude D. J., Ellison D. C., Nagataki S., Slane P. O., 2014, *ApJ*, **791**, 97
- Lee S.-H., Patnaude D. J., Raymond J. C., Nagataki S., Slane P. O., Ellison D. C., 2015, *ApJ*, **806**, 71
- Lee Y.-H., Koo B.-C., Lee J.-J., Burton M. G., Ryder S., 2019, arXiv e-prints, p. [arXiv:1902.03847](https://arxiv.org/abs/1902.03847)
- Lopez L. A., Fesen R. A., 2018, *Space Sci. Rev.*, **214**, 44
- Lopez L. A., Ramirez-Ruiz E., Pooley D. A., Jeltema T. E., 2009a, *ApJ*, **691**, 875
- Lopez L. A., Ramirez-Ruiz E., Badenes C., Huppenkothen D., Jeltema T. E., Pooley D. A., 2009b, *ApJ*, **706**, L106
- Lopez L. A., Ramirez-Ruiz E., Huppenkothen D., Badenes C., Pooley D. A., 2011, *ApJ*, **732**, 114

- Lopez L. A., Ramirez-Ruiz E., Castro D., Pearson S., 2013a, *ApJ*, **764**, 50
- Lopez L. A., Pearson S., Ramirez-Ruiz E., Castro D., Yamaguchi H., Slane P. O., Smith R. K., 2013b, *ApJ*, **777**, 145
- Lopez L. A., et al., 2015, *ApJ*, **814**, 132
- Maoz D., Mannucci F., Nelemans G., 2014, *ARA&A*, **52**, 107
- Martínez-Rodríguez H., et al., 2017, *ApJ*, **843**, 35
- Martínez-Rodríguez H., et al., 2018, *ApJ*, **865**, 151
- Matsumura H., Tanaka T., Uchida H., Okon H., Tsuru T. G., 2017, *ApJ*, **851**, 73
- McWilliam A., Piro A. L., Badenes C., Bravo E., 2018, *ApJ*, **857**, 97
- Miceli M., Bocchino F., Decourchelle A., Ballet J., Reale F., 2010, *A&A*, **514**, L2
- Ohnishi T., Uchida H., Tsuru T. G., Koyama K., Masai K., Sawada M., 2014, *ApJ*, **784**, 74
- Ozawa M., Koyama K., Yamaguchi H., Masai K., Tamagawa T., 2009, *ApJ*, **706**, L71
- Park S., et al., 2013, *ApJ*, **767**, L10
- Patnaude D., Badenes C., 2017, Supernova Remnants as Clues to Their Progenitors. p. 2233, doi:10.1007/978-3-319-21846-5_98
- Patnaude D. J., Ellison D. C., Slane P., 2009, *ApJ*, **696**, 1956
- Patnaude D. J., Slane P., Raymond J. C., Ellison D. C., 2010, *ApJ*, **725**, 1476
- Patnaude D. J., Badenes C., Park S., Laming J. M., 2012, *ApJ*, **756**, 6
- Patnaude D. J., Lee S.-H., Slane P. O., Badenes C., Heger A., Ellison D. C., Nagataki S., 2015, *ApJ*, **803**, 101
- Patnaude D. J., Lee S.-H., Slane P. O., Badenes C., Nagataki S., Ellison D. C., Milisavljevic D., 2017, *ApJ*, **849**, 109
- Pérez F., Granger B. E., 2007, *Computing in Science and Engineering*, **9**, 21
- Peters C. L., Lopez L. A., Ramirez-Ruiz E., Stassun K. G., Figueroa-Feliciano E., 2013, *ApJ*, **771**, L38
- Price-Whelan A. M., et al., 2018, preprint, (arXiv:1801.02634)
- Ranasinghe S., Leahy D. A., 2018, *AJ*, **155**, 204
- Rest A., et al., 2005, *Nature*, **438**, 1132
- Rest A., et al., 2008a, *ApJ*, **680**, 1137
- Rest A., et al., 2008b, *ApJ*, **681**, L81
- Reynolds S. P., Borkowski K. J., Hwang U., Hughes J. P., Badenes C., Laming J. M., Blondin J. M., 2007, *ApJ*, **668**, L135
- Rho J., Petre R., 1998, *ApJ*, **503**, L167
- Safi-Harb S., Petre R., Arnaud K. A., Keohane J. W., Borkowski K. J., Dyer K. K., Reynolds S. P., Hughes J. P., 2000, *ApJ*, **545**, 922
- Safi-Harb S., Dubner G., Petre R., Holt S. S., Durouchoux P., 2005, *ApJ*, **618**, 321
- Sano H., et al., 2018, *ApJ*, **867**, 7
- Sato T., et al., 2020, *ApJ*, **893**, 49
- Shappee B. J., et al., 2014, *ApJ*, **788**, 48
- Smartt S. J., 2009, *ARA&A*, **47**, 63
- Smith R. M., et al., 2014, in Ground-based and Airborne Instrumentation for Astronomy V. p. 914779, doi:10.1117/12.2070014
- Sukhbold T., Ertl T., Woosley S. E., Brown J. M., Janka H.-T., 2016, *ApJ*, **821**, 38
- Tananbaum H., 1999, IAU Circ., **7246**
- Tawa N., et al., 2008, *PASJ*, **60**, S11
- Tonry J. L., et al., 2018, *PASP*, **130**, 064505
- Uchida H., et al., 2012, *Publications of the Astronomical Society of Japan*, **64**, 141
- Van Der Walt S., Colbert S. C., Varoquaux G., 2011, preprint, (arXiv:1102.1523)
- Vink J., 2012, *A&ARv*, **20**, 49
- Wilms J., Allen A., McCray R., 2000, *ApJ*, **542**, 914
- Woods T. E., Ghavamian P., Badenes C., Gilfanov M., 2017, *Nature Astronomy*, **1**, 263
- Woods T. E., Ghavamian P., Badenes C., Gilfanov M., 2018, preprint, (arXiv:1807.03798)
- Yamaguchi H., Ozawa M., Koyama K., Masai K., Hiraga J. S., Ozaki M., Yonetoku D., 2009, *ApJ*, **705**, L6
- Yamaguchi H., et al., 2014a, *ApJ*, **780**, 136
- Yamaguchi H., et al., 2014b, *ApJ*, **785**, L27
- Yamaguchi H., et al., 2015, *ApJ*, **801**, L31
- Zhou P., Vink J., 2018, *A&A*, **615**, A150
- Zhou P., Chen Y., Zhang Z.-Y., Li X.-D., Safi-Harb S., Zhou X., Zhang X., 2016, *ApJ*, **826**, 34
- Zoglauer A., et al., 2015, *ApJ*, **798**, 98